The Astrophysical Journal Letters, 904:L18 (7pp), 2020 December 1 https://doi.org/10.3847/2041-8213/abc704

Hiding Signatures of Gravitational Instability in Protoplanetary Disks with Planets

Sahl Rowther[1,2], Farzana Meru[1,2], Grant M. Kennedy[1,2], Rebecca Nealon[3], and Christophe Pinte[4]
[1] Centre for Exoplanets and Habitability, University of Warwick, Coventry CV4 7AL, UK; sahl.rowther@warwick.ac.uk
[2] Department of Physics, University of Warwick, Coventry CV4 7AL, UK
[3] Department of Physics and Astronomy, University of Leicester, Leicester LE1 7RH, UK
[4] School of Physics and Astronomy, Monash University, Clayton, Vic 3800, Australia
Received 2020 September 4; revised 2020 October 23; accepted 2020 November 3; published 2020 November 26

Abstract

We carry out three-dimensional smoothed particle hydrodynamics simulations to show that a migrating giant planet strongly suppresses the spiral structure in self-gravitating disks. We present mock Atacama Large Millimeter/submillimeter Array (ALMA) continuum observations that show that in the absence of a planet, spiral arms due to gravitational instability are easily observed. Whereas in the presence of a giant planet, the spiral structures are suppressed by the migrating planet resulting in a largely axisymmetric disk with a ring and gap structure. Our modeling of the gas kinematics shows that the planet's presence could be inferred, for example, using optically thin $^{13}C^{16}O$. Our results show that it is not necessary to limit the gas mass of disks by assuming high dust-to-gas mass ratios in order to explain a lack of spiral features that would otherwise be expected in high-mass disks.

Unified Astronomy Thesaurus concepts: Protoplanetary disks (1300)

1. Introduction

In the past few years, a large number of disks have revealed substructure in the form of rings and gaps when observed at millimeter wavelengths with the Atacama Large Millimeter/submillimeter Array (ALMA; ALMA Partnership et al. 2015; Andrews et al. 2016, 2018; Dipierro et al. 2018; Fedele et al. 2018; Huang et al. 2018; Booth & Ilee 2020). A few of these disks are thought to be very young (<1 Myr; ALMA Partnership et al. 2015; Fedele et al. 2018; Dipierro et al. 2018). Ring and gap structures have also been observed in even younger ($\lesssim$0.5 Myr) Class 1 disks (Sheehan & Eisner 2018; Segura-Cox et al. 2020). Young disks are thought to be massive and could potentially be gravitationally unstable. Such disks are expected to harbor spiral arms. There is evidence that disks with spiral arms in the midplane exist (Pérez et al. 2016; Huang et al. 2018), although they seem to be quite rare. Is the observed rarity due to young disks being less massive or can spiral structures in massive disks be hidden by other processes?

The goal of this Letter is to investigate the impact that a migrating giant planet, irrespective of how it formed, has on the structure of a gravitationally unstable disk and the resulting implications for observations of such disks. We find that a migrating giant planet is able to suppress spiral structures yielding disks that appear axisymmetric with rings and gaps.

2. Method

2.1. Hydrodynamical Simulations and Initial Conditions

We perform scale-free 3D gas hydrodynamic simulations using PHANTOM, a smoothed particle hydrodynamics (SPH) code developed by Price et al. (2018).

The disk setup is identical to that in Rowther & Meru (2020). We model a disk using 2 million particles between $R_{\rm in} = 1$ and $R_{\rm out} = 25$ in code units with a disk-to-star mass ratio of 0.1. The central star and the planet are modeled as sink particles (Bate et al. 1995). The accretion radius of the central star is set to be equal to the disk inner boundary, $R_{\rm in}$. To maintain a roughly constant planet mass throughout the simulation, the accretion radius of the planet is limited by setting it to 0.001 in code units. This is ~10 times smaller than the minimum Hill radius for a $3M_{\rm Jup}$ planet at $R_{\rm in}$. The initial surface mass density is set as a smoothed power law and is given by

$$\Sigma = \Sigma_0 \left(\frac{R}{R_0}\right)^{-1} f_s, \tag{1}$$

where Σ_0 is the surface mass density at $R = R_0 = 1$ and $f_s = 1 - \sqrt{R_{\rm in}/R}$ is the factor used to smooth the surface density at the inner boundary of the disk. The initial temperature profile is expressed as a power law

$$T = T_0 \left(\frac{R}{R_0}\right)^{-0.5}, \tag{2}$$

where T_0 is set such that the disk aspect ratio $H/R = 0.05$ at $R = R_0$. The energy equation is

$$\frac{du}{dt} = -\frac{P}{\rho}(\nabla \cdot \boldsymbol{v}) + \Lambda_{\rm shock} - \frac{\Lambda_{\rm cool}}{\rho}, \tag{3}$$

where we assume an adiabatic equation of state, u is the specific internal energy, the first term on the right-hand side is the PdV work, $\Lambda_{\rm shock}$ is a heating term that is due to the artificial viscosity used to correctly deal with shock fronts, and

$$\Lambda_{\rm cool} = \frac{\rho u}{t_{\rm cool}} \tag{4}$$

controls the cooling in the disk. Here we use a simple implementation of the cooling time that is proportional to the dynamical time by a factor of β,

$$t_{\rm cool} = \beta(R)\Omega^{-1} = \beta_0 \left(\frac{R}{R_0}\right)^{-2} \Omega^{-1}, \tag{5}$$

where Ω is the orbital frequency and we have varied β with radius (Rowther & Meru 2020). This allows us to mimic a realistic self-gravitating disk that is only gravitationally unstable in the outer regions (Rafikov 2005; Clarke 2009; Rice & Armitage 2009; Stamatellos & Whitworth 2009).

To model shocks, we use an artificial viscosity switch that utilizes the time derivative of the velocity divergence introduced by Cullen & Dehnen (2010). The artificial viscosity parameter α_v has a maximum of $\alpha_{\rm max} = 1$ near the shock and a minimum of $\alpha_{\rm min} = 0$ far away from the shock. The artificial viscosity coefficient β_v is set to 2 (see Price et al. 2018).

2.1.1. Embedding the Planet

The simulation is first run for 10 orbits to allow spiral structure in the disk to develop. We then split it into two simulations, one with an embedded planet and one that continues to evolve without a planet. The latter is a control simulation to compare the impact a migrating giant planet has on the spiral structure in a gravitationally unstable disk. A planet with a planet-to-star mass ratio of $q = 2.9 \times 10^{-3}$, equivalent to $3M_{\rm Jup}$ in a $0.1M_\odot$ disk around a $1M_\odot$ central star is added at $R_{\rm p} = 20$.

The simulations are run for another 8 orbits, with a total simulation time of 18 orbits.

2.2. Postprocessing of Simulations

The raw synthetic continuum images at 1.3 mm are created using MCFOST (Pinte et al. 2006, 2009). We first scale the simulations such that $R_{\rm out} = 200$ au, and initial $R_{\rm p} = 160$ au. We use 10^8 photon packets on a Voronoi tesselation where each MCFOST cell corresponds to an SPH particle. The luminosity of the star is calculated using an assumed mass of $1M_\odot$ and a 1 Myr isochrone from Siess et al. (2000) that corresponds to a temperature of $T_\star = 4286$ K. Since the gas surface density of the disk is quite large, the Stokes numbers in the disk are small enough (<0.1 for millimeter-sized grains) that we assume that the dust is well coupled to gas. Therefore, we assume that the dust distribution is identical to the gas distribution and a constant dust-to-gas ratio of 0.01. The dust sizes vary between 0.3 and 1000 μm and are distributed across 100 different sizes with a power-law exponent of -3.5. We assume all dust grains are made of astronomical silicates, and are spherical and homogeneous. We compute the dust properties using Mie theory. The disk is assumed to be at a distance of 140 pc.

To create mock millimeter continuum observations, we use the ALMA Observation Support Tool (Heywood et al. 2011). We use integration times of 12, 30, 60, and 120 minutes at 230 GHz (1.3 mm) in Band 6 with the ALMA Cycle 8 C43-7 configuration. We assume a bandwidth of 7.5 GHz and a precipitable water vapor level of 0.913 mm. CLEAN images are created using natural weights resulting in a beam size of $0\farcs107 \times 0\farcs124$ or, equivalently, 15.0 au $\times$ 17.3 au at 140pc. As shown by Mayer et al. (2016), different ALMA configurations can alter the detectability of features. Hence, a similar set of mock observations are created with the C43-6 configuration ($0\farcs156 \times 0\farcs196$) and with a disk inclined at 40° using the C43-7 configuration.

Assuming a disk inclination and position angle of 40°, optically thick ^{12}CO, and optically thinner ^{13}C^{16}O CO-isotopologue channel maps are generated for the $J = 3 - 2$ transition using a velocity resolution of 0.1 km s^{-1}. We choose this transition as it can be observed with a good compromise between observation time and signal-to-noise ratio. The abundances for ^{12}CO and ^{13}C^{16}O are assumed to be a fraction 1×10^{-4} and 2×10^{-7} of the total disk mass (i.e., relative to H_2), respectively. We account for CO freezeout at $T < 20$ K, and photodissociation and photodesorption in regions of high UV radiation (see Appendix B of Pinte et al. 2018). We then convolve the resulting images with a beam size of $0\farcs05 \times 0\farcs05$, the maximum resolution expected for CO line observations.

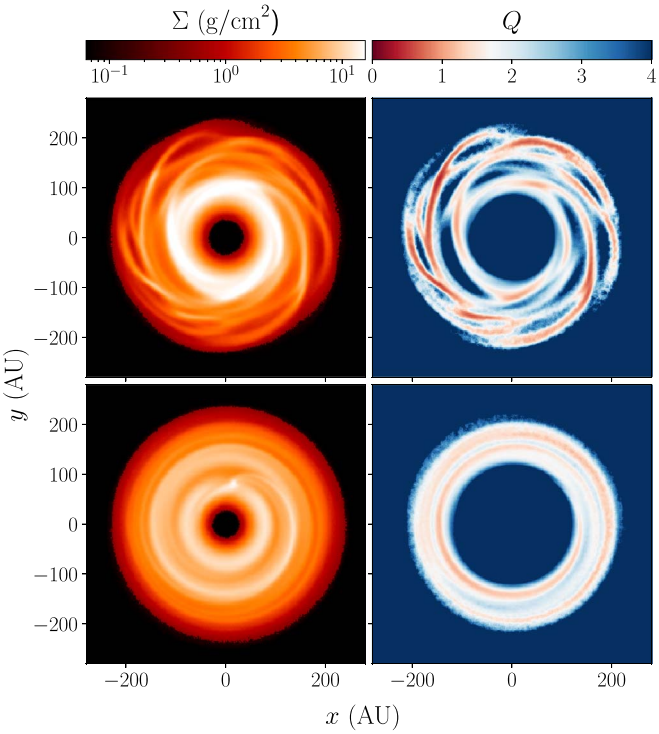

Figure 1. Surface density (left) and 2D Toomre parameter (right) plots of a disk without a planet (top) and with a $3M_{\rm Jup}$ planet (bottom) at the end of the simulation. The 2D Toomre plots show how gravitationally unstable the disk is. The critical value for nonaxisymmetric instabilities is when $Q \lesssim 1.7$ (Durisen et al. 2007), shown in red. The planet erases the spiral structure and is massive enough to carve out a gap. This results in a gravitationally stable axisymmetric disk.

3. Results

3.1. Impact on Spiral Structure

As shown in Rowther & Meru (2020), planets migrate inward rapidly until they reach the gravitationally stable inner disk. For the simulations presented here, the gravitationally stable region is inside $R \approx 120$ au. The impact of the planet on the disk as it migrates is compared to the control simulation using the Toomre parameter (Toomre 1964),

$$Q = \frac{c_s \Omega}{\pi G \Sigma}, \tag{6}$$

which gives a measure of how gravitationally unstable the disk is, where Σ and c_s are the disk surface density and sound speed, respectively.

Figure 1 shows the surface density (left) and the 2D Toomre parameter Q (right) of the simulations without a planet (top) and with a $3M_{\rm Jup}$ planet (bottom) at the end of the simulation. It is clear that the presence of the planet significantly impacts the structure. The planet suppresses the spiral structure and opens up a gap. Despite both disks retaining the same disk mass ($\sim 0.09M_\odot$) within 200 au, the 2D Q plots show that the presence of the planet results in the disk becoming mostly

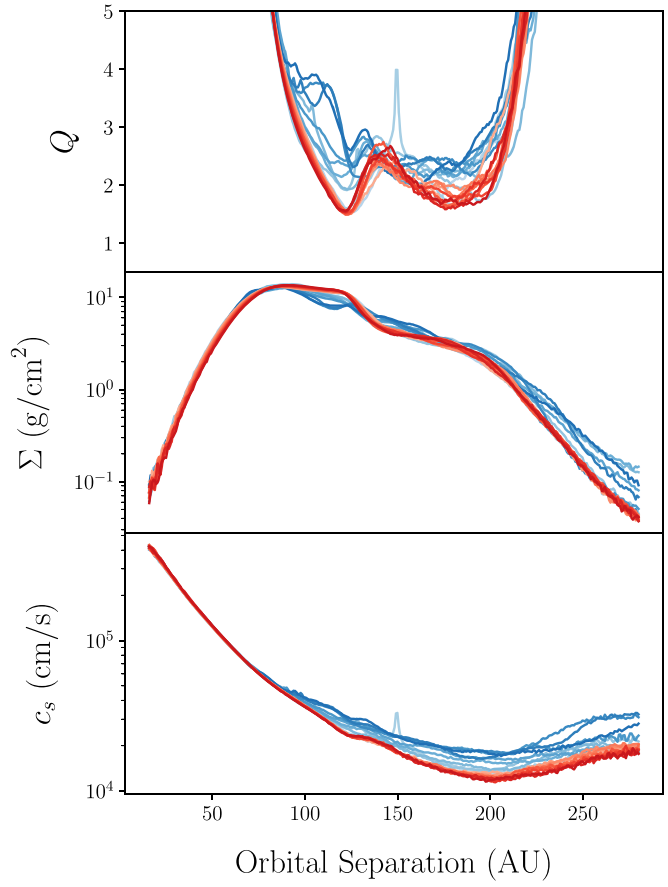

Figure 2. Azimuthally averaged Toomre parameter, Q (top), surface density, Σ (middle), and the sound speed, c_s (bottom) for both the disk without a planet (red lines) and with a $3M_{\rm Jup}$ planet (blue lines) for the first two orbits after the planet is added. The darker shades represent later times. The increase in c_s due to the planet is the dominant reason for the increase in Q in the outer regions of the disk (beyond $R \approx 120$ au), causing the disk to become gravitationally stable.

gravitationally stable with $Q > 1.7$ throughout the disk. Without a planet, strong gravitationally unstable ($Q < 1.7$) arms are present.

The dominant reason for the increase in Q is due to the planet's influence on the disk temperature, or equivalently the sound speed c_s, in the disk. The spiral wakes generated by the planet as it migrates are regions of relative overdensities with respect to the disk background. The radially propagating spiral wakes can evolve into shocks. The exchange of momentum and energy between the density wakes and the disk at the shocks influence the global properties of the disk, heating it up (Goodman & Rafikov 2001; Rafikov 2016; Ziampras et al. 2020).

The azimuthally averaged Toomre parameter (top), surface density (middle), and sound speed (bottom) are plotted in Figure 2 for the first two orbits after the $3M_{\rm Jup}$ planet (blue lines) is embedded. The red lines represent the disk without the planet at the same times. It can be seen, particularly in the regions of the disk beyond $R \approx 120$ au, that there is a quick and significant increase in the sound speed after the planet has been added, whereas the change in Σ is relatively small. This increase in temperature causes the disk to become gravitationally stable, resulting in a higher value of the Toomre parameter.

To ensure the sudden inclusion of the $3M_{\rm Jup}$ planet did not trigger artificial excess heating, we compared the artificial viscosity to the gravitational stress parameter immediately after the planet was embedded. The increase in artificial viscosity due to the planet is negligible compared to the magnitude of the gravitational stress parameter.

3.2. Continuum Images

The left column of Figure 3 compares the mock observations of a disk with a $3M_{\rm Jup}$ planet (bottom) and without a planet (top) with an integration time of 30 minutes using the C43-7 configuration. An axisymmetric flux map is produced as the azimuthally averaged flux of the mock observations and is shown in the middle column. Finally to highlight nonaxisymmetric features, the residual flux is plotted in the right column by subtracting the axisymmetric map from the mock observation. The top subset of panels in Figure 4 show the mock observations (top half) and residuals (bottom half) using the higher-resolution C43-7 configuration. The bottom left subset of panels show the same, but with the lower-resolution C43-6 configuration. The bottom right subset of panels are for a disk inclined by 40° using the C43-7 configuration.

From Figure 3, it can be seen that without a planet, spiral arms due to gravitational instability would be readily apparent. Whereas with the planet, the only major nonaxisymmetric feature that remains is the spiral arms caused by the planet as shown in Figures 3 and 4. The higher-resolution mock observations are able to better resolve the gap; however, the planet-induced spiral arms are only visible with integration times >1 hr. This is true for both the noninclined and moderately inclined disk. Using a lower resolution, which increases the signal to noise, allows the spiral arms to be easily seen in the residuals at lower integration times. The tradeoff is a gap that is less resolved and shallower in the continuum image. Despite the lower-resolution images showing the spiral arms of the planet more easily, higher-resolution images would still be favorable as a less resolved and shallower gap can lead to underestimates of the planet's mass. This could in turn lead to predictions with other methods of estimating the planet's mass, such as with the CO kinematics, that are inconsistent.

3.3. CO Kinematics

The spiral waves generated by the planet can cause localized deviations in the Keplerian flow of the disk as shown recently by Pinte et al. (2019, 2020). These deviations can be detected as *kinks* in the gas channel maps.

Figure 5 shows the channel maps for ^{12}CO and ^{13}C^{16}O at $\Delta v = \pm 0.5$ km s^{-1} from the systemic velocity with the continuum subtracted. The optically thick ^{12}CO does not reveal any signs of a planet, but a kink is noticeable in the optically thinner ^{13}C^{16}O in the -0.5 km s^{-1} channel within the vicinity of the planet. We can exclude large-scale perturbations or any azimuthally symmetric mechanisms since the kink is not seen in the opposite velocity channel where the profile remains smooth. The kink is shown in the bottom right panel of Figure 5(b) in the inset. The kink is also seen in the channels from $v = -0.3$ to -1.2 km s^{-1}.

Although the channel maps without the planet are not perfectly smooth as would be expected from a Keplerian disk, this is likely to be due to the gravitational instabilities. Hall et al. (2020) show that for a gravitationally unstable disk the perturbations due to gravitational instabilities are seen in all azimuths and in both the positive and negative velocity

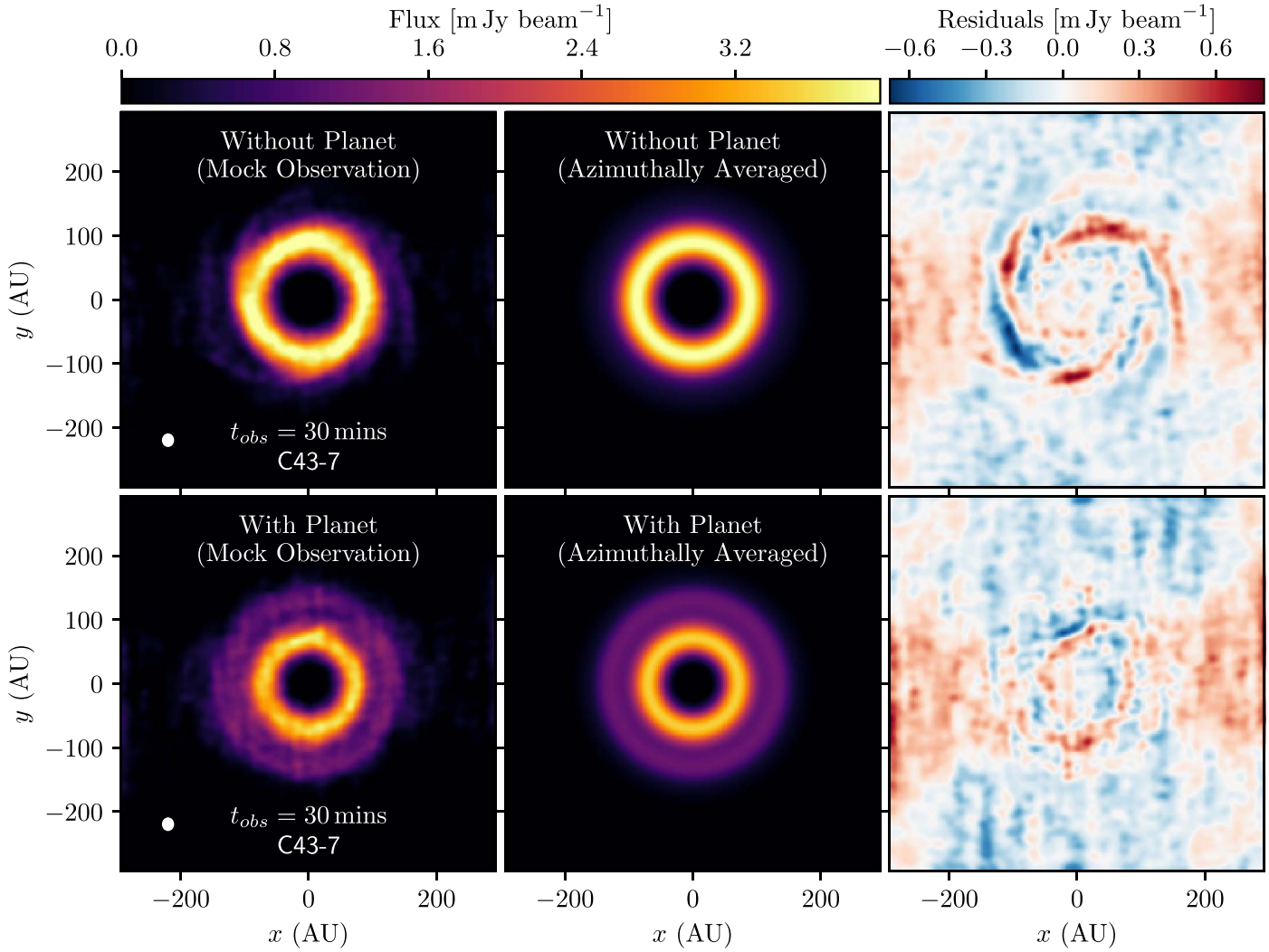

Figure 3. Mock observation (left) using the C43-7 configuration with an integration time of 30 minutes, axisymmetric flux map (middle), and residual flux (right) of a disk without a planet (top) and with a $3M_{\rm Jup}$ planet (bottom). The white ellipse in the bottom left of each mock observation represents the beam size. The presence of the planet results in a disk that no longer consists of spiral structure due to gravitational instability and appears to be more axisymmetric.

channels. However, in our simulations with a planet, the kink is more localized appearing in only the negative velocity channel. To ensure that the observed kink is due to the planet, we recalculated the channel maps with the planet at slightly different times with the planet being in different azimuthal locations. Although the kink is not detectable at all times, whenever the kink is detected it is in a different location determined by the position of the planet. Additionally, in some cases the kink was only detected for a narrower range of Δv.

4. Discussion

4.1. Implications for Dust-to-gas Mass Ratios

In the early stages of evolution, disks are expected to be massive and gravitationally unstable (e.g., Bate 2018). A characteristic feature of such disks are their spiral arms. However, from observations so far (Pérez et al. 2016; Huang et al. 2018), these disks appear to be quite rare. Due to the difficulty in directly measuring the gas mass of the disk, the disk mass is often inferred via the dust mass using a fixed dust-to-gas mass ratio. In some scenarios, such as with MWC 480 (Liu et al. 2019), the observed dust mass can be high enough such that inferring the gas mass via the canonical dust-to-gas mass ratio of 0.01 results in a disk that is massive enough to be gravitationally unstable. Thus, in their models, they assume a higher dust-to-gas mass ratio to ensure that the disk is gravitationally stable. Facchini et al. (2020) show that LkCa-15 retains a significant amount of dust mass in its rings. Consequently, when modeling LkCa-15, they assume an upper limit on the disk gas mass (and hence a higher dust-to-gas mass ratio) to ensure the disk is not locally gravitationally unstable.

In both cases this assumption was deemed necessary to explain the lack of spiral features in the observations, which would be expected from more massive disks. However, we show that a migrating $3M_{\rm Jup}$ planet can cause a massive disk to become gravitationally stable and suppress any spiral structure that would otherwise be present. Hence, large dust-to-gas mass ratios are not necessarily required to explain a lack of spiral features.

4.2. Caveats

A caveat to the results presented here is the long-term gravitational stability of the disks due to the cooling mechanism used. Although it mimics the characteristics of a realistic self-gravitating disk, i.e., a disk that is only

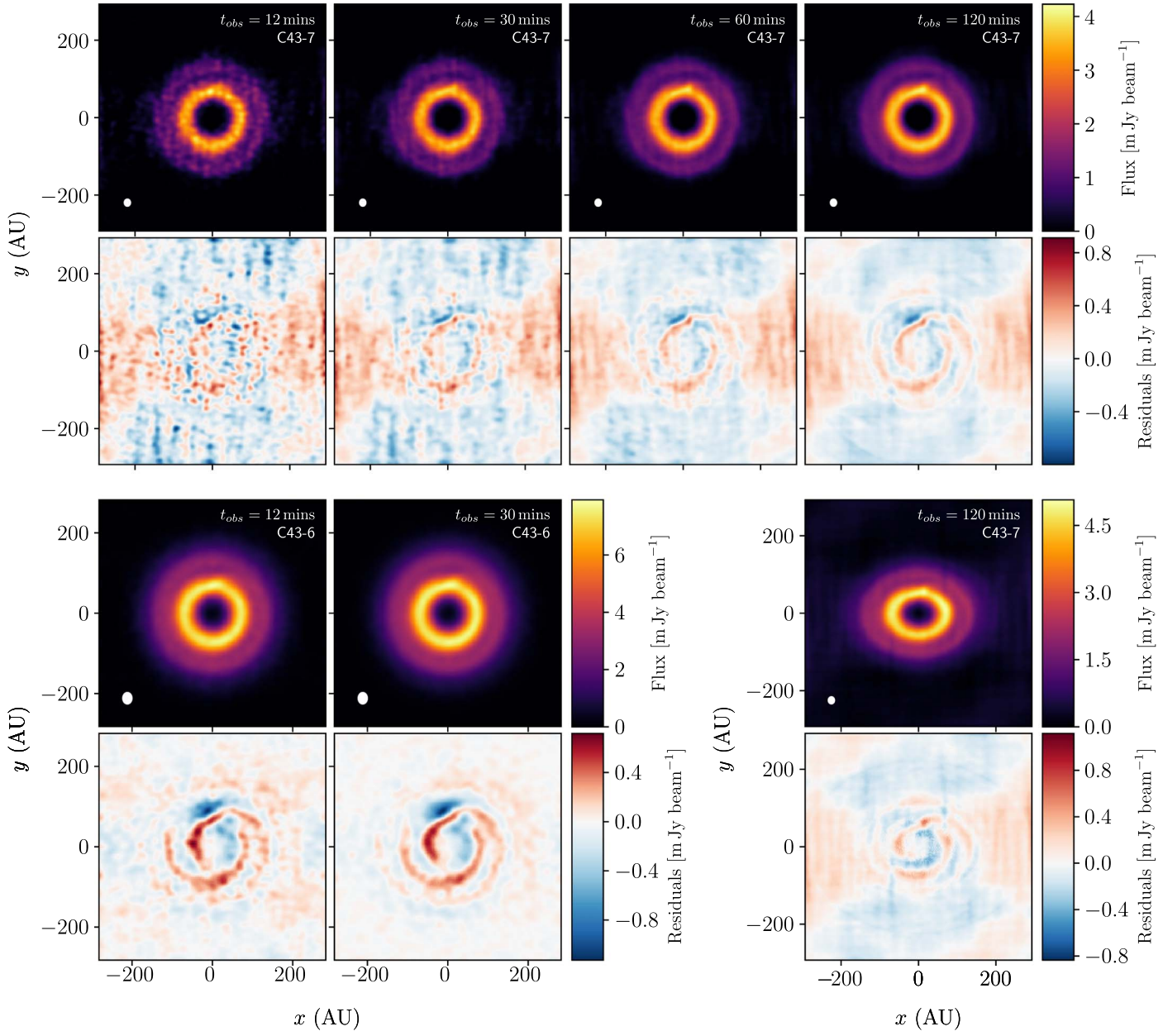

Figure 4. Top subset of panels shows the mock observations (top half) and residual plots (bottom half) of a disk with a $3M_{\rm Jup}$ planet with integration times of 12, 30, 60, and 120 minutes using the higher-resolution C43-7 configuration. The bottom left subset of panels is similar but only for integrations times of 12 and 30 minutes using the C43-6 configuration. At high resolution the disk appears completely axisymmetric with short integration times. Whereas with longer integration times (over 60 minutes), spiral arms caused by the planet can be seen in the residual plots. At lower resolutions, the gap carved by the planet appears shallower, but the planet's spiral arms are easier to detect even with short integration times. The bottom right subset of panels show that the planet's spiral arms are also detectable for moderately inclined disks. This is shown for a disk inclined by 40°.

gravitationally unstable in the outer regions, it is still a straightforward implementation where the cooling time is a simple expression determined by the location in the disk.

The actual cooling in the disk is likely to be more complex and evolve over time. Recently Mercer et al. (2018) calculated an effective β from their radiative transfer calculations, which was found to vary both spatially and with time. Hence, it is unknown what impact using more complex cooling methods such as radiative transfer to cool the disk will have on the long-term gravitational stability of the disk with a migrating planet. While we show that a migrating giant planet can erase the spiral structure in a self-gravitating disk, it remains to be investigated whether the loss of spiral structure remains for a significant amount of time.

The results presented here initially appear contrary to Meru (2015) where it was shown that a fragment formed by gravitational instability in the outer disk could trigger subsequent fragmentation in the inner disk. The main difference is that the Toomre profiles are quite different. In Meru (2015), the inner disk was on the edge of fragmentation ($Q \sim 1$). Hence, the increase in the surface density as a result of the fragment driving material inward toward the disk caused the disk to fragment. This behavior is not seen or expected in this work as the inner disk remains well above the gravitationally stable regime ($Q \gtrsim 1.7$).

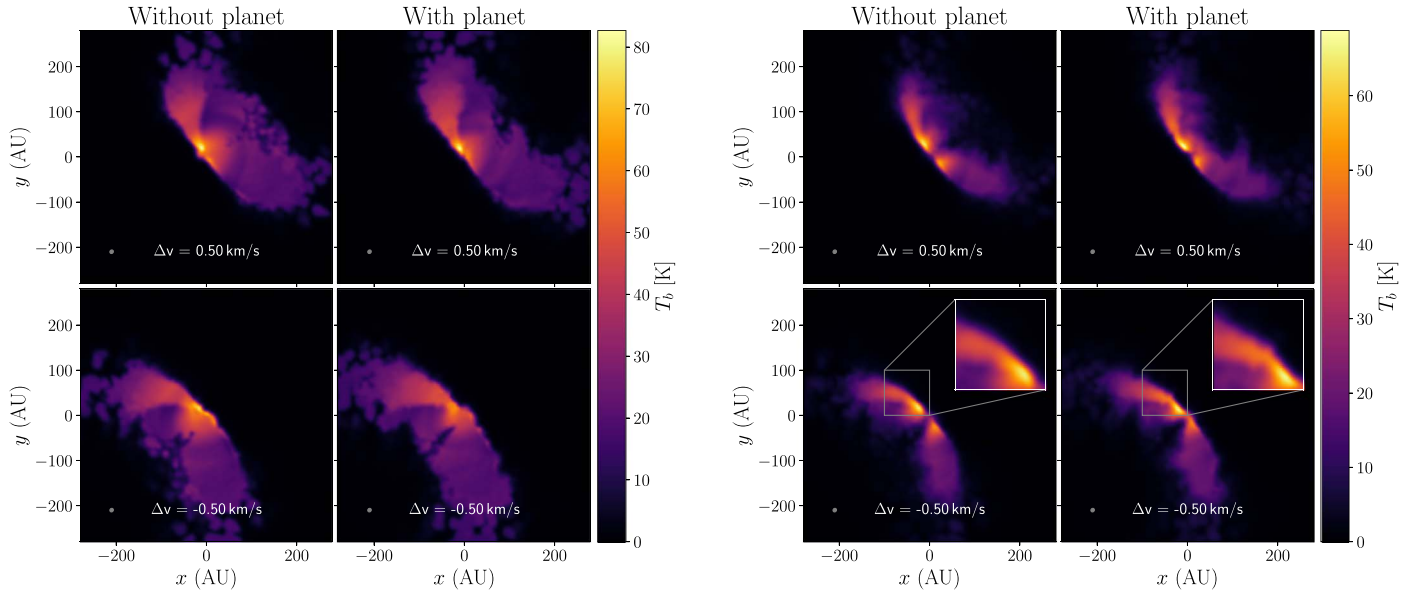

(a) ^{12}CO (b) $^{13}C^{16}O$

Figure 5. Synthetic continuum-subtracted channel maps ($J = 3 - 2$ transitions) for (a) ^{12}CO and (b) $^{13}C^{16}O$ at $\Delta v = \pm$ 0.5 km s^{-1} from the systemic velocity of the disk with and without the planet. A kink is not detected in the optically thick ^{12}CO, but is visible in the optically thin $^{13}C^{16}O$ in the negative velocity channel within the vicinity of the planet; see bottom right inset in panel (b). The bend in the velocity profile in the bottom right inset is referred to as the kink. This is contrasted with the smooth velocity profile in the bottom left inset. The disk inclination and position angle are both 40°.

In this work, we have only presented results for one planet and disk mass. Lower-mass planets would be less likely to impact self-gravitating spiral structures. On the other hand, lower-mass disks, which have weaker gravitational instabilities, would be more susceptible to having their spiral structures suppressed by planets. Although we find that a planet that is large enough to open up a gap also suppresses the spiral structure, we cannot conclude that non-gap-opening planets are unable to affect the disk structure. We will present a follow-up study that considers a variety of planet and disk properties, as well as ALMA configurations, to investigate the conditions at which spiral suppression is likely to be observed.

5. Conclusion

We perform 3D SPH simulations to investigate the impact a migrating giant planet has on the structure of a gravitationally unstable disk. Our work shows that the presence of the planet suppresses the spiral structure in the disk and causes the disk to become gravitationally stable because it alters the temperature structure. This interaction between the planet and the disk causes the self-gravitating phase of the disk to be shortened, while retaining the same disk mass. The planet is able to carve open a gap resulting in an axisymmetric disk.

The mock ALMA observations of the continuum presented here show that the disk can appear completely axisymmetric for higher-resolution ALMA configurations. However, with longer integration times or by sacrificing resolution, spiral arms from the planet become observable. In the latter case, the gap carved by the planet will be less resolved and appear shallower. We also show that the planet can be detected with high resolution kinematics using optically thin CO-isotopologues like $^{13}C^{16}O$. Our results show it is possible to explain a lack of spiral structure in high-mass disks without requiring high dust-to-gas mass ratios to limit the gas mass.

We thank the anonymous referee for their useful comments that benefited this work. S.R. acknowledges support from the Royal Society Enhancement Award. F.M. acknowledges support from the Royal Society Dorothy Hodgkin Fellowship. G.M.K. is supported by the Royal Society as a Royal Society University Research Fellow. R.N. acknowledges funding from the European Research Council (ERC) under the European Union's Horizon 2020 research and innovation program (grant agreement No. 681601). C.P. acknowledges funding from the Australian Research Council via FT170100040 and DP180104235. This work was performed using Orac and Tinis HPC clusters at the University of Warwick.

Software: Matplotlib (Hunter 2007), numpy (van der Walt et al. 2011), astropy (The Astropy Collaboration et al. 2018), PHANTOM (Price et al. 2018), SPLASH (Price 2007), MCFOST (Pinte et al. 2006, 2009).

ORCID iDs

Sahl Rowther https://orcid.org/0000-0003-4249-4478
Farzana Meru https://orcid.org/0000-0002-3984-9496
Grant M. Kennedy https://orcid.org/0000-0001-6831-7547
Rebecca Nealon https://orcid.org/0000-0003-0856-679X
Christophe Pinte https://orcid.org/0000-0001-5907-5179

References

Andrews, S. M., Huang, J., Pérez, L. M., et al. 2018, ApJL, 869, L41
Andrews, S. M., Wilner, D. J., Zhu, Z., et al. 2016, ApJL, 820, L40
Bate, M. R. 2018, MNRAS, 475, 5618
Bate, M. R., Bonnell, I. A., & Price, N. M. 1995, MNRAS, 277, 362
Booth, A. S., & Ilee, J. D. 2020, MNRAS, 493, L108
ALMA Partnership, Brogan, C. L., Pérez, L. M., et al. 2015, ApJL, 808, L3
Clarke, C. J. 2009, MNRAS, 396, 1066
Cullen, L., & Dehnen, W. 2010, MNRAS, 408, 669
Dipierro, G., Ricci, L., Pérez, L., et al. 2018, MNRAS, 475, 5296

Durisen, R. H., Boss, A. P., Mayer, L., et al. 2007, in Protostars and Planets V, ed. B. Reipurth, D. Jewitt, & K. Keil (Tucson, AZ: Univ. Arizona Press), 607
Facchini, S., Benisty, M., Bae, J., et al. 2020, A&A, 639, A121
Fedele, D., Tazzari, M., Booth, R., et al. 2018, A&A, 610, A24
Goodman, J., & Rafikov, R. R. 2001, ApJ, 552, 793
Hall, C., Dong, R., Teague, R., et al. 2020, arXiv:2007.15686
Heywood, I., Avison, A., & Williams, C. J. 2011, arXiv:1106.3516
Huang, J., Andrews, S. M., Dullemond, C. P., et al. 2018, ApJL, 869, L42
Hunter, J. D. 2007, CSE, 9, 90
Liu, Y., Dipierro, G., Dagusa, E., et al. 2019, A&A, 622, A75
Mayer, L., Peters, T., Pineda, J. E., Wadsley, J., & Rogers, P. 2016, ApJL, 823, L36
Mercer, A., Stamatellos, D., & Dunhill, A. 2018, MNRAS, 478, 3478
Meru, F. 2015, MNRAS, 454, 2529
Pérez, L. M., Carpenter, J. M., Andrews, S. M., et al. 2016, Sci, 353, 1519
Pinte, C., Harries, T. J., Min, M., et al. 2009, A&A, 498, 967
Pinte, C., Ménard, F., Duchêne, G., et al. 2018, A&A, 609, A47
Pinte, C., Ménard, F., Duchêne, G., & Bastien, P. 2006, A&A, 459, 797
Pinte, C., Price, D. J., Ménard, F., et al. 2020, ApJL, 890, L9
Pinte, C., van der Plas, G., Ménard, F., et al. 2019, NatAs, 3, 1109
Price, D. J. 2007, PASA, 24, 159
Price, D. J., Wurster, J., Tricco, T. S., et al. 2018, PASA, 35, e031
The Astropy Collaboration, Price-Whelan, A. M., Sipőcz, B. M., et al. 2018, AJ, 156, 123
Rafikov, R. R. 2005, ApJL, 621, L69
Rafikov, R. R. 2016, ApJ, 831, 122
Rice, W. K. M., & Armitage, P. J. 2009, MNRAS, 396, 2228
Rowther, S., & Meru, F. 2020, MNRAS, 496, 1598
Segura-Cox, D. M., Schmiedeke, A., Pineda, J. E., et al. 2020, Natur, 586, 228
Sheehan, P. D., & Eisner, J. A. 2018, ApJ, 857, 18
Siess, L., Dufour, E., & Forestini, M. 2000, A&A, 358, 593
Stamatellos, D., & Whitworth, A. P. 2009, in AIP Conf. Ser. 1094, Proc. 15th Cambridge Workshop on Cool Stars, Stellar Systems, and the Sun, ed. E. Stempels (Melville, NY: AIP), 557
Toomre, A. 1964, ApJ, 139, 1217
van der Walt, S., Colbert, S. C., & Varoquaux, G. 2011, CSE, 13, 22
Ziampras, A., Ataiee, S., Kley, W., Dullemond, C. P., & Baruteau, C. 2020, A&A, 633, A29